Determination of k′−J′ Correlations of Reaction Products by Fluorescence-Imaging Techniques. 1. Linearly Polarized Excitation Scheme

Kuo-mei Chen* and Jia-lin Chang

Department of Chemistry, National Sun Yat-sen University, Kaohsiung, Taiwan, Republic of China

Received: August 19, 1996; In Final Form: December 11, 1996[⊗]

A one-photon excited fluorescence detection scheme that employs fluorescence-imaging techniques is proposed to determine **k′**−**J′** correlations of reaction products. To extract information of **k′**−**J′** correlations from the fluorescence intensities of image patterns, a density matrix formalism is utilized to analyze both the linearly polarized and the circularly polarized detection schemes of a one-photon excited fluorescence process, in which a linearly polarized excitation laser is employed. Explicit fluorescence intensity formulas are given for various detection schemes and transition sequences. For the detection scheme that probes linearly polarized fluorescence photons, state multipoles of the density matrix of reaction products along various scattering angles θ, that is, population ($\rho_0^0(\theta)$) and alignment parameters ($\rho_0^2(\theta)$, $\rho_1^2(\theta)$, $\rho_2^2(\theta)$, $\rho_0^4(\theta)$, $\rho_1^4(\theta)$, $\rho_2^4(\theta)$, $\rho_3^4(\theta)$, $\rho_4^4(\theta)$), can be uniquely determined by 12 independent measurements of the intensities of fluorescence imagings as functions of probe angles and transition sequences. Experiments which measure circularly polarized fluorescence photons can provide information on orientation parameters ($\rho_1^1(\theta)$, $\rho_1^3(\theta)$, $\rho_3^3(\theta)$) in the present detection scheme. Contributions of the individual term in the intensity formulas to the fluorescence imagings have been assessed by numerical calculations. A pattern recognition of fluorescence images of photofragments with **v**−**J** correlations has also been established.

I. Introduction

Correlations of vector quantities of products from photofragmentation processes or chemical reactions have fascinated the scientific community in chemical dynamics.[1−3] Since the pioneer studies by Herschbach and co-workers,[4−6] researchers have recognized the important role of vector correlations in probing detailed dynamics of molecular collisions. In particular, Case et al.[6] have analyzed the laser-induced fluorescence (LIF) process of a polarized ensemble. In recent years, optical detection, especially Doppler spectroscopy,[7−11] has been heavily emphasized to reveal the **v**−**J** correlations[1−3] of reaction products. Dixon[12] and Hall et al.[13] have independently developed theoretical frameworks to analyze Doppler profiles in terms of bipolar moments or elements of the density matrix of photofragments.

In a series of investigations, Zare and co-workers[14−19] have established a complete formalism to determine population, orientation, and alignment moments of reaction products by LIF or resonance-enhanced multiphoton ionization (REMPI) detection schemes. Correlations of angular momenta with other vectorial observables have not been treated explicitly in these works. Recently, Orr-Ewing, Simons, Hall, and co-workers have employed Doppler spectroscopy to study vector correlations in photo-initiated bimolecular reactions.[20−25] Zare and coworkers have demonstrated the power of the REMPI detection scheme in the study of state-to-state differential cross sections[26−29] and the three-dimensional (3D) velocity distribution of products[30] in photo-initiated bulb reactions. A theoretical framework that deals with the problem of the angular momentum polarization of products in these photo-initiated reactions has been reported by Shafer-Ray et al.[31]

Instead of projecting all the 3D information on angular distributions and angular momentum polarizations in a specific quantum state onto the probe laser direction from an expanding Newton sphere of reaction products, one can employ alternatively two-dimensional (2D) ion-imaging techniques[32,33] or the slicing technique of fluorescence imaging[34−38] in the study of reaction dynamics. In the present report, we propose a one-photon excited fluorescence (1 + 1 LIF) detection scheme to determine **k′**−**J′** correlations of reaction products. From detailed analyses, we will show that **k′**−**J′** correlations are best studied by fluorescence imaging to avoid an average of detected signals over spatial profiles of product distributions.

In section II, density matrix theory for polarized reaction products is reviewed. Our proposed detection scheme is elucidated in section III. The theoretical framework is developed in subsequent sections to acquire useful formulas for fluorescence intensity as a function of experimental parameters. To assess the contribution of the individual term in the intensity formulas to the fluorescence image pattern, numerical results of these intensity factors under various experimental conditions are reported. To illustrate the application of the present formalism, the simulated fluorescence image patterns in a 1 + 1 LIF detection scheme are presented for photofragments with either a cartwheel motion (**v** ⊥ **J**) or a helicopter motion (**v** ∥ **J**).

II. Density Matrix of Reaction Products

To treat the polarization properties of optical transitions and molecular ensembles, the density matrix formalism[3,39−44] has been proven to be a powerful theoretical tool. In the present section, we consider a distribution of reaction products in a specific quantum state over a Newton sphere, where the expansion rate of such a sphere is determined by the conservation of energy. In a polarized photodissociation experiment under crossed laser beam−molecular beam conditions, the angular distribution of photofragments on the Newton sphere should display an axial symmetry with respect to the polarization direction of the photolysis laser, provided that the precursors in the molecular beam are unaligned. It is well-known that the centers of the expanding Newton spheres of photofragments move at velocities identical to those of their precursors.

[⊗] Abstract published in *Advance ACS Abstracts,* March 1, 1997.

S1089-5639(96)02546-7 CCC: $14.00

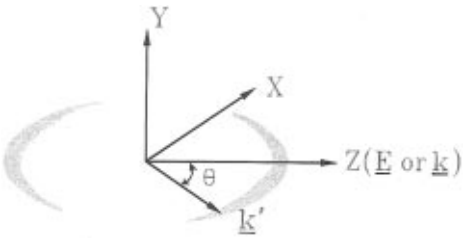

Figure 1. Sliced section of the Newton sphere of reaction products.

Realizing the moving direction of the center of the Newton sphere and its axially symmetric axis, one should slice the sphere with a laser sheet along a unique plane defined by the polarization direction of the photolysis laser and the moving direction of the parent molecules. Adopting this slicing scheme, we can obtain useful information of angular distributions, recoil velocities, and angular momentum polarizations of photofragments in the center-of-mass frame.[34,35] Similarly, one should slice the Newton sphere of reaction products along the crossing plane in a crossed beam chemical reaction, in which the angular distribution of products on the Newton sphere displays an axial symmetry with respect to the relative velocity vector.

In Figure 1, we depict an instantaneous pattern of number densities of product A in a specific quantum state from a sliced section of the Newton sphere at a chosen delay time, in conjunction with a reference coordinate system, where product A is generated either by a photofragmentation process AB $\xrightarrow{h\nu}$ A + B or a bimolecular reaction C + D → A + B. The *Z*-axis of this space-fixed frame (SFF) is defined along either the polarization direction **E** of the photolysis laser in a photodissociation experiment or the relative velocity vector **k** in a crossed beam chemical reaction. For product A scattered along **k′**, the number density function $N(\hat{\mathbf{k}}\cdot\hat{\mathbf{k}}') = N(\cos\theta) \equiv N(\theta)$ represents the angular distribution, where the caret denotes a unit vector and θ is the angle between **k** and **k′**. Alternatively, $N(\theta)$ is a legitimate measurement on **k**−**k′** (or **E**−**k′**) correlations.

The internal state distribution of product A over the magnetic sublevels can display polarization properties. Assuming that the ground state product A has populations in an angular momentum state $|aJ_1M_1\rangle$, one can expand its density matrix $\rho_g(\theta)$ in terms of the irreducible tensor operator $T^{(k_1)}_{q_1}(aJ_1,aJ_1)$

$$\rho_g(\theta) = \sum_{k_1q_1} {}^g\rho^{k_1}_{q_1}(\theta)T^{(k_1)}_{q_1}(aJ_1,aJ_1) \tag{1}$$

where ${}^g\rho^{k_1}_{q_1}(\theta)$ is a state multipole[40] and quantum number *a* is a label of the state vector other than the angular momenta. In general, the product angular momentum **J′** displays correlations with respect to the recoil direction **k′**. Naturally, one should denote the density matrix ρ_g as a function of θ. In the above equation, $T^{(k_1)}_{q_1}(aJ_1,aJ_1)$ is defined by[40]

$$T^{(k_1)}_{q_1}(aJ_1,aJ_1) = \sum_{M_1M_1'} (-1)^{J_1-M_1}\hat{k}_1 \begin{pmatrix} J_1 & J_1 & k_1 \\ M_1 & -M_1' & -q_1 \end{pmatrix} |aJ_1M_1\rangle\langle aJ_1M_1'| \tag{2}$$

where $\hat{k}_1 = (2k_1 + 1)^{1/2}$ and

$$\begin{pmatrix} \cdot & \cdot & \cdot \\ \cdot & \cdot & \cdot \end{pmatrix}$$

is a 3-*j* symbol.[41]

It should be noted that the slicing technique of fluorescence imaging destroys the cylindrical symmetry of internal state distributions; that is, molecules which are probed by the laser sheet are only a subset of the original ensemble. Thus, we have to examine the inherent symmetry consequences of the collisional process. For nonchiral reactants, the scattering plane defined by **k** and **k′** displays a symmetry of reflection invariance. From the basic properties of the density matrix under reflection in the scattering plane, we have[40]

$${}^g\rho^k_q = (-1)^{k+q}\,{}^g\rho^k_{-q} \tag{3}$$

and

$${}^g\rho^k_q = (-1)^k\,{}^g\rho^k_q{}^* \tag{4}$$

It is straightforward to derive that ${}^g\rho^k_q$ is real when *k* is even, ${}^g\rho^k_q$ is purely imaginary when *k* is odd, and ${}^g\rho^k_0(k{=}\text{odd}) = 0$. For a 1 + 1 LIF detection scheme, state multipoles from $k = 0$ up to $k = 4$ can be determined in principle.[14] From the above two equations, we will focus on the functional dependences of ${}^g\rho^0_0(\theta)$, $i^g\rho^1_1(\theta)$ $(=i^g\rho^1_{-1}(\theta))$, ${}^g\rho^2_0(\theta)$, ${}^g\rho^2_1(\theta)$ $(=-{}^g\rho^2_{-1}(\theta))$, ${}^g\rho^2_2(\theta)$ $(={}^g\rho^2_{-2}(\theta))$, $i^g\rho^3_1(\theta)(=i^g\rho^3_{-1}(\theta))$, $i^g\rho^3_2(\theta)(=-i^g\rho^3_{-2}(\theta))$, $i^g\rho^3_3(\theta)(=i^g\rho^3_{-3}(\theta))$, ${}^g\rho^4_0(\theta)$, ${}^g\rho^4_1(\theta)(=-{}^g\rho^4_{-1}(\theta))$, ${}^g\rho^4_2(\theta)(={}^g\rho^4_{-2}(\theta))$, ${}^g\rho^4_3(\theta)(=-{}^g\rho^4_{-3}(\theta))$, and ${}^g\rho^4_4(\theta)(={}^g\rho^4_{-4}(\theta))$ on experimental parameters. In total, there are 13 independent state multipoles to be determined in a 1 + 1 LIF imaging experiment.[4,45] Among them, $i^g\rho^1_1(\theta)$, $i^g\rho^3_1(\theta)$, $i^g\rho^3_2(\theta)$, and $i^g\rho^3_3(\theta)$ are imaginary numbers. The alignment parameters $A^{(k)}_q$ which have been commonly adopted in the literature on angular momentum polarizations are proportional to the corresponding state multipoles with the same rank and component. The relationship between $A^{(k)}_q$ and ρ^k_q can be found in a review article by Orr-Ewing and Zare.[3]

III. Detection Scheme of k′−J′ Correlations

A schematic diagram of the proposed detection scheme of **k′**−**J′** correlations of reaction products is depicted in Figure 2a. The propagation direction (along the unit vector $\hat{\mathbf{U}}_P$) of the probe laser sheet, the polarization direction of a linearly polarized photolysis laser beam (along the unit vector $\hat{\mathbf{E}}$), and the orientation of a 2D imaging detector (along the unit vector $\hat{\mathbf{U}}_i$) are mutually orthogonal to each other. By mounting an appropriate set of polarizers in front of the imaging detector, we can take fluorescence images using either linearly or circularly polarized photons. For a crossed beam bimolecular reaction, $\hat{\mathbf{E}}$ is replaced by the relative velocity unit vector $\hat{\mathbf{k}}$. The probe laser is linearly polarized, and its polarization direction makes an angle χ with respect to the $\hat{\mathbf{E}} - \hat{\mathbf{U}}_P$ plane. The transformation between the probe laser reference frame and the SFF is depicted in Figure 2b.

To simplify the sequence of frame transformations, the quantization axis of products is defined to be the polarization direction of the photolysis laser or the relative velocity vector, no matter which recoil direction $\hat{\mathbf{k}}'$ is. In other words, the Euler angles which transform the SFF to a reference frame with its *Z′*-axis along the polarization direction of the probe laser sheet are ($\pi/2$, χ, 0) for every recoil direction $\hat{\mathbf{k}}'$ (see Figure 2b). Because the density matrix $\rho_g(\theta)$ is a function of the scattering angle θ, this convention of the quantization axis does not lose its generality in our framework development.

From the above analysis, the **k′**−**J′** correlations are measurements of the variation of angular momentum polarizations of products with respect to the recoil direction **k′**. In subsequent sections, we will prove that the experimental determination of the state multipoles of the density matrix relies on the functional dependences of fluorescence images with respect to the probe angle χ, the polarization states of fluorescence photons, and the transition sequence in the 1 + 1 LIF. The key procedure of

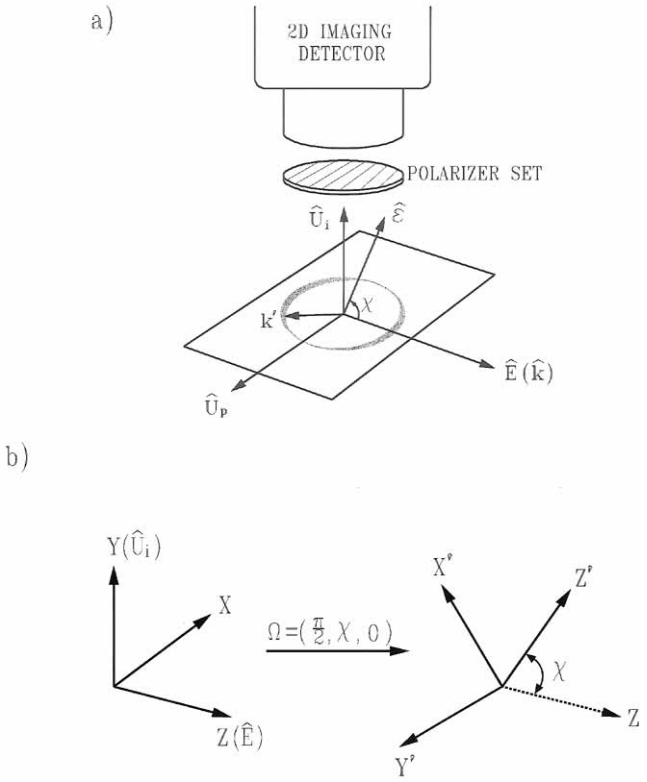

Figure 2. (a) Schematic diagram of experimental arrangement to study **k′−J′** correlations of reaction products. (b) Transformation between the probe laser reference frame and the SFF.

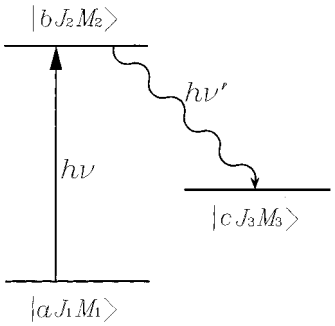

Figure 3. Energy level diagram in a 1 + 1 LIF detection scheme.

this detection scheme is to monitor the intensity variations of the image patterns from a specific transition sequence by rotating the polarization direction of the probe laser sheet.

IV. Density Matrix of the Excited State

The energy level diagram which illustrates the 1 + 1 LIF detection scheme is depicted in Figure 3. The probe laser is tuned to induce the transition $|bJ_2M_2\rangle \leftarrow |aJ_1M_1\rangle$ of product A, while spontaneous emissions from $|bJ_2M_2\rangle \rightarrow |cJ_3M_3\rangle$ are monitored. In the reference frame defined by the probe laser (see Figure 2b), $\rho_g(\theta)$ in eq 1 is transformed to[41]

$$\rho_g(\theta) = \sum_{k_1q_1q_2} {}^g\rho_{q_1}^{k_1}(\theta)\, D_{q_1q_2}^{k_1}\left(\frac{\pi}{2},\chi,0\right)^* \tilde{T}_{q_2}^{(k_1)}(aJ_1,aJ_1)$$

$$= \sum_{k_1q_1q_2} {}^g\rho_{q_1}^{k_1}(\theta)\, \exp(i\pi q_1/2)\, d_{q_1q_2}^{k_1}(\chi)\, \tilde{T}_{q_2}^{(k_1)}(aJ_1,aJ_1) \qquad (5)$$

where the tensor operator $\tilde{T}_{q_2}^{(k_1)}(aJ_1,aJ_2)$ is defined in a reference frame with its quantization axis along the polarization direction of the probe laser. In the above equation, $d_{q_1q_2}^{k_1}$ is a reduced rotation matrix.[41]

For an optical transition $|bJ_2M_2\rangle \leftarrow |aJ_1M_1\rangle$, the excited state density matrix $\rho_e(\theta)$ is[42−44]

$$\rho_e(\theta) = \hat{\epsilon}\cdot\mathbf{r}\rho_g(\theta)\,(\hat{\epsilon}\cdot\mathbf{r})^\dagger$$

$$= \sum_{\substack{k_1q_1q_2\\M_1M_1'}} (-1)^{J_1-M_1}\hat{k}_1\begin{pmatrix}J_1 & J_1 & k_1\\ M_1 & -M_1' & -q_2\end{pmatrix} {}^g\rho_{q_1}^{k_1}(\theta)\times$$

$$\exp(i\pi q_1/2)\, d_{q_1q_2}^{k_1}(\chi)\, \hat{\epsilon}\cdot\mathbf{r}|aJ_1M_1\rangle\langle aJ_1M_1'|(\hat{\epsilon}\cdot\mathbf{r})^\dagger \quad (6)$$

where $\hat{\epsilon}\cdot\mathbf{r}$ is a transition dipole operator. $\rho_e(\theta)$ can be expanded in terms of the irreducible tensor operator $\tilde{T}_{q_3}^{(k_2)}(bJ_2,bJ_2)^\dagger$. From eq 6, the state multipole ${}^e\rho_{q_3}^{k_2}(\theta)$ is given by

$${}^e\rho_{q_3}^{k_2}(\theta) = \sum_{\substack{k_1q_1q_2\\M_1M_1'M_2M_2'}} (-1)^{J_1+J_2-M_1-M_2}\hat{k}_1\hat{k}_2\begin{pmatrix}J_1 & J_1 & k_1\\ M_1 & -M_1' & -q_2\end{pmatrix}\times$$

$$\begin{pmatrix}J_2 & J_2 & k_2\\ M_2 & -M_2' & -q_3\end{pmatrix}\langle bJ_2M_2'|\hat{\epsilon}\cdot\mathbf{r}|aJ_1M_1\rangle\times$$

$$\langle aJ_1M_1'|(\hat{\epsilon}\cdot\mathbf{r})^\dagger|bJ_2M_2\rangle\exp(i\pi q_1/2)\, d_{q_1q_2}^{k_1}(\chi)\, {}^g\rho_{q_1}^{k_1}(\theta) \quad (7)$$

For a linearly polarized probe laser, $\hat{\epsilon}\cdot\mathbf{r} = r_0 = \sum_t D_{0t}^1(\Omega)^*\,\tilde{r}_t$, where $\tilde{r}_t$ is a spherical dipole operator in a molecule-fixed frame. If the product A is a symmetric top, the state vector $|aJ_1M_1\rangle = |a\rangle|J_1K_1M_1\rangle = (-1)^{M_1-K_1}[(2J_1+1)/8\pi^2]^{1/2}D_{-M_1-K_1}^{J_1}(\Omega)|a\rangle$, where $|a\rangle$ is a vibronic wave function of the ground electronic state. From angular momentum algebra, one can prove easily that the matrix element $\langle bJ_2M_2'|\hat{\epsilon}\cdot\mathbf{r}|aJ_1M_1\rangle$ is[42−44]

$$\langle bJ_2M_2'|\hat{\epsilon}\cdot\mathbf{r}|aJ_1M_1\rangle =$$

$$\sum_t (-1)^{M_1-K_1+t}\hat{J}_1\hat{J}_2\begin{pmatrix}J_2 & 1 & J_1\\ M'_2 & 0 & -M_1\end{pmatrix}\times$$

$$\begin{pmatrix}J_2 & 1 & J_1\\ K_2 & -t & -K_1\end{pmatrix}\langle b|\tilde{r}_t|a\rangle \quad (8)$$

From eqs 7 and 8, one has

$${}^e\rho_{q_3}^{k_2}(\theta) = \sum_{\substack{k_1q_1q_2\\M_1M_1'M_2M_2'}} (-1)^{J_1+J_2}\hat{k}_1\hat{k}_2\hat{J}_1{}^2\hat{J}_2{}^2\begin{pmatrix}J_1 & J_1 & k_1\\ M_1 & -M_1' & -q_2\end{pmatrix}\times$$

$$\begin{pmatrix}J_2 & J_2 & k_2\\ M_2 & -M'_2 & -q_3\end{pmatrix}\begin{pmatrix}J_2 & 1 & J_1\\ M'_2 & 0 & -M_1\end{pmatrix}\times$$

$$\begin{pmatrix}J_2 & 1 & J_1\\ M_2 & 0 & -M_1'\end{pmatrix}|m_1|^2\exp(i\pi q_1/2)\, d_{q_1q_2}^{k_1}(\chi)\, {}^g\rho_{q_1}^{k_1}(\theta) \quad (9)$$

where $|m_1|^2$ is a transition amplitude of the product A and

$$|m_1|^2 = \sum_t\begin{pmatrix}J_2 & 1 & J_1\\ K_2 & -t & -K_1\end{pmatrix}^2|\langle b|\tilde{r}_t|a\rangle|^2 \qquad (10)$$

The selection rules on ΔK can be read directly from the above equation for parallel ($t = 0$) or perpendicular transitions ($t = \pm 1$).

The sum over the magnetic quantum numbers of the product of four 3-j symbols in eq 9 can be contracted by angular momentum algebra. One can prove easily that[41]

$$\rho_e(\theta) = \sum_{\substack{k_1k_2x\\q_1q_2}} (-1)^{k_2+1}\hat{k}_1\hat{k}_2\hat{J}_1{}^2\hat{J}_2{}^2\hat{x}^2\begin{pmatrix}k_1 & x & k_2\\ -q_2 & 0 & q_2\end{pmatrix} \times$$
$$\begin{pmatrix}x & 1 & 1\\ 0 & 0 & 0\end{pmatrix}\begin{Bmatrix}k_1 & k_2 & x\\ J_1 & J_2 & 1\\ J_1 & J_2 & 1\end{Bmatrix}|m_1|^2 \times$$
$$\exp(i\pi q_1/2)\, d^{k_1}_{q_1q_2}(\chi)\, {}^g\rho^{k_1}_{q_1}(\theta)\, \tilde{T}^{(k_2)}_{-q_2}(bJ_2,bJ_2)^\dagger \quad (11)$$

where

$$\begin{Bmatrix}\cdot & \cdot & \cdot\\ \cdot & \cdot & \cdot\\ \cdot & \cdot & \cdot\end{Bmatrix}$$

is a 9-j symbol.[41] From the transformation properties of $\rho_g(\theta)$ and $\hat{\epsilon}\cdot\mathbf{r}$ under a symmetry operation of reflection in the $X'-Y'$ plane (see Figure 2b), one can prove that a constraint has to impose on $\rho_e(\theta)$, that is, the sum of rank indices, $k_1 + k_2$, must be an even, positive integer for the present excitation scheme.

For later developments, we transform $\tilde{T}^{(k_2)}_{-q_2}(bJ_2,bJ_2)^\dagger$ back to the SFF. From the transformation properties of tensor operators, we have[41]

$$\rho_e(\theta) = \sum_{\substack{k_1k_2x\\q_1q_2q_3}} (-1)^{k_2+1}\hat{k}_1\hat{k}_2\hat{J}_1{}^2\hat{J}_2{}^2\hat{x}^2\begin{pmatrix}k_1 & x & k_2\\ -q_2 & 0 & q_2\end{pmatrix} \times$$
$$\begin{pmatrix}x & 1 & 1\\ 0 & 0 & 0\end{pmatrix}\begin{Bmatrix}k_1 & k_2 & x\\ J_1 & J_2 & 1\\ J_1 & J_2 & 1\end{Bmatrix}|m_1|^2 \times$$
$$\exp[i\pi(q_1+q_3)/2]\, d^{k_1}_{q_1q_2}(\chi)\, d^{k_2}_{q_3,-q_2}(\chi)\, {}^g\rho^{k_1}_{q_1}(\theta)\, T^{(k_2)}_{q_3}(bJ_2,bJ_2)^\dagger \quad (12)$$

The above equation can be simplified further by contracting the rotation matrices and employing the orthorgonality relationship of 3-j symbols. Thus, we have

$$\rho_e(\theta) = \sum_{\substack{k_1k_2x\\q_1q_3}} (-1)^{k_2+1}\hat{k}_1\hat{k}_2\hat{J}_1{}^2\hat{J}_2{}^2\hat{x}^2\begin{pmatrix}k_1 & k_2 & x\\ q_1 & q_3 & -q_1-q_3\end{pmatrix} \times$$
$$\begin{pmatrix}x & 1 & 1\\ 0 & 0 & 0\end{pmatrix}\begin{Bmatrix}k_1 & k_2 & x\\ J_1 & J_2 & 1\\ J_1 & J_2 & 1\end{Bmatrix}|m_1|^2 \times$$
$$\exp[i\pi(q_1+q_3)/2]\, d^{x}_{-q_1-q_3,0}(\chi)\, {}^g\rho^{k_1}_{q_1}(\theta)\, T^{(k_2)}_{q_3}(bJ_2,bJ_2)^\dagger \quad (13)$$

Examining the 3-j symbol

$$\begin{pmatrix}x & 1 & 1\\ 0 & 0 & 0\end{pmatrix}$$

in the above equation, we realize that x must be 0 or 2. Accordingly, the final form of the excited state density matrix in the SFF is given by

$$\rho_e(\theta) = \sum_{k_1q_1}(-1)^{J_1+J_2+k_1+q_1+1}\, 3^{-1}\hat{J}_1{}^2\hat{J}_2{}^2\begin{Bmatrix}J_1 & J_1 & k_1\\ J_2 & J_2 & 1\end{Bmatrix} \times$$
$$|m_1|^2\, {}^g\rho^{k_1}_{q_1}(\theta)\, T^{(k_1)}_{-q_1}(bJ_2,bJ_2)^\dagger + \sum_{\substack{k_1k_2\\q_1q_3}}(-1)^{k_2+1}\left(\frac{10}{3}\right)^{1/2}\hat{k}_1\hat{k}_2\hat{J}_1{}^2\hat{J}_2{}^2 \times$$
$$\begin{pmatrix}k_1 & k_2 & 2\\ q_1 & q_3 & -q_1-q_3\end{pmatrix}\begin{Bmatrix}k_1 & k_2 & 2\\ J_1 & J_2 & 1\\ J_1 & J_2 & 1\end{Bmatrix}|m_1|^2 \times$$
$$\exp[i\pi(q_1+q_3)/2]\, d^{2}_{-q_1-q_3,0}(\chi)\, {}^g\rho^{k_1}_{q_1}(\theta)\, T^{(k_2)}_{q_3}(bJ_2,bJ_2)^\dagger \quad (14)$$

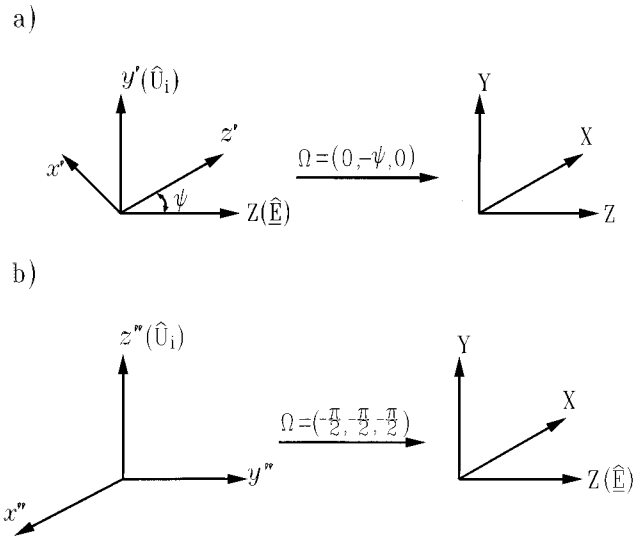

Figure 4. (a) Transformation between the reference frame of the linearly polarized detection mode and the SFF. (b) Transformation between the reference frame of the circularly polarized detection mode and the SFF.

where

$$\begin{Bmatrix}\cdot & \cdot & \cdot\\ \cdot & \cdot & \cdot\end{Bmatrix}$$

is a 6-j symbol.[41]

V. Fluorescence Detection Operator

To detect the transition $|bJ_2M_2\rangle \rightarrow |cJ_3M_3\rangle$, one has to set up the fluorescence detection operator $F(\hat{\epsilon}_d)$[42−44] before taking the trace of the product $\rho_e(\theta)F$. $F(\hat{\epsilon}_d)$ is given by

$$F(\hat{\epsilon}_d) = \hat{J}_3^{-2}\sum_{M_3}\hat{\epsilon}_d\cdot\mathbf{r}|cJ_3M_3\rangle\langle cJ_3M_3|(\hat{\epsilon}_d\cdot\mathbf{r})^\dagger \quad (15)$$

The fluorescence detection operator $F(\hat{\epsilon}_d)$ can be expanded in terms of the irreducible tensor operators $T^{(k_3)}_{q_3}(bJ_2,bJ_2)$. These tensor operators are expressed in the same basis functions as those of $\rho_e(\theta)$; in addition, $\rho_e(\theta)$ and $F(\hat{\epsilon}_d)$ have to be defined in an identical reference frame when $Tr[\rho_eF]$ is taken. Thus, we should examine the reference frames of various detection schemes and their Euler angles of transformations to the SFF. In Figure 4a, we depict an $x'y'z'$-frame for the detection mode of linearly polarized fluorescence photons. The z'-axis is the direction of the polarization direction, while the propagation direction of fluorescence photons is along the y'-axis. The Euler angles which transform the $x'y'z'$-frame back to the SFF are (0, $-\psi$, 0), where ψ is the angle between the z' and Z-axis. Similarly, an $x''y''z''$-frame for the detection mode of circularly polarized fluorescence photons is depicted in Figure 4b. The propagation direction of fluorescence photons is along the z''-axis in this mode. To transform the $x''y''z''$-frame to the SFF, the Euler angles are ($-\pi/2$, $-\pi/2$, $-\pi/2$).

A. Linearly Polarized Detection Mode. In the detection frame, the dipole transition operator is

$$\hat{\epsilon}_d\cdot\mathbf{r} = r_q = \sum_t D^1_{qt}(\Omega)^*\tilde{r}_t \quad (16)$$

where $q = 0$ and ±1 denote linearly polarized and circularly polarized photons, respectively. Using a similar procedure presented in section IV, we can prove that

$$\bar{F}(\mathrm{lpp},\psi) = \sum_k (-1)^{J_2+J_3}\hat{k}\hat{J}_2^2\begin{pmatrix}1 & 1 & k\\ 0 & 0 & 0\end{pmatrix}\times \begin{Bmatrix}1 & 1 & k\\ J_2 & J_2 & J_3\end{Bmatrix}|m_2|^2\bar{T}_0^{(k)}(bJ_2,bJ_2)$$

$$= \left[\frac{1}{3}\hat{J}_2\bar{T}_0^{(0)} + (-1)^{J_2+J_3}\left(\frac{2}{3}\right)^{1/2}\hat{J}_2^2\begin{Bmatrix}1 & 1 & 2\\ J_2 & J_2 & J_3\end{Bmatrix}\times \bar{T}_0^{(2)}\right]|m_2|^2 \quad (17)$$

where $\bar{F}$ and $\bar{T}_0^{(k)}$ are defined in the $x'y'z'$-frame and lpp denotes the linearly polarized detection mode. For brevity, we have denoted $\bar{T}_0^{(k)}(bJ_2,bJ_2)$ by $\bar{T}_0^{(k)}$. In the above equation, the transition amplitude $|m_2|^2$ is given by

$$|m_2|^2 = \sum_t \begin{pmatrix}J_2 & 1 & J_3\\ K_2 & -t & -K_3\end{pmatrix}^2 |\langle b|\tilde{r}_t|c\rangle|^2 \quad (18)$$

After transforming $\bar{F}$ back to the SFF, we obtain

$$F(\mathrm{lpp},\psi) = \left[\frac{1}{3}\hat{J}_2T_0^{(0)} + (-1)^{J_2+J_3}\left(\frac{1}{2}\right)\hat{J}_2^2\begin{Bmatrix}1 & 1 & 2\\ J_2 & J_2 & J_3\end{Bmatrix}\times \sin^2\psi\,(T_2^{(2)} + T_{-2}^{(2)}) + (-1)^{J_2+J_3+1}\hat{J}_2^2\begin{Bmatrix}1 & 1 & 2\\ J_2 & J_2 & J_3\end{Bmatrix}\times \sin\psi\cos\psi\,(T_1^{(2)} - T_{-1}^{(2)}) + (-1)^{J_2+J_3}\left(\frac{1}{6}\right)^{1/2}\hat{J}_2^2\times \begin{Bmatrix}1 & 1 & 2\\ J_2 & J_2 & J_3\end{Bmatrix}(3\cos^2\psi - 1)T_0^{(2)}\right]|m_2|^2 \quad (19)$$

For an unpolarized detection mode, we can sum the contributions of two mutually orthogonal, linearly polarized detection operators. Accordingly, we have

$$F(\mathrm{unpol}) = F(\mathrm{lpp},\psi{=}0) + F(\mathrm{lpp},\psi{=}{}^{\pi}/_2) = \left\{\frac{2}{3}\hat{J}_2T_0^{(0)} + (-1)^{J_2+J_3}\hat{J}_2^2\begin{Bmatrix}1 & 1 & 2\\ J_2 & J_2 & J_3\end{Bmatrix}\left[\frac{1}{2}(T_2^{(2)} + T_{-2}^{(2)}) + \left(\frac{1}{6}\right)^{1/2}T_0^{(2)}\right]\right\}|m_2|^2 \quad (20)$$

B. Circularly Polarized Detection Mode. For the left circularly polarized detection mode, we can prove that

$$\bar{\bar{F}}(\mathrm{cpp,L}) = \sum_k (-1)^{J_2+J_3+1}\hat{k}\hat{J}_2^2\begin{pmatrix}1 & 1 & k\\ -1 & 1 & 0\end{pmatrix}\times \begin{Bmatrix}1 & 1 & k\\ J_2 & J_2 & J_3\end{Bmatrix}|m_2|^2\,\bar{\bar{T}}_0^{(k)}$$

$$= \left[\frac{1}{3}\hat{J}_2\bar{\bar{T}}_0^{(0)} + (-1)^{J_2+J_3}\left(\frac{1}{2}\right)^{1/2}\hat{J}_2^2\begin{Bmatrix}1 & 1 & 1\\ J_2 & J_2 & J_3\end{Bmatrix}\times \bar{\bar{T}}_0^{(1)} + (-1)^{J_2+J_3+1}\left(\frac{1}{6}\right)^{1/2}\hat{J}_2^2\begin{Bmatrix}1 & 1 & 2\\ J_2 & J_2 & J_3\end{Bmatrix}\bar{\bar{T}}_0^{(2)}\right]|m_2|^2 \quad (21)$$

where $\bar{\bar{F}}$ and $\bar{\bar{T}}_0^{(k)}$ are defined in the $x''y''z''$-frame and cpp denotes the circularly polarized detection mode. After transforming $\bar{\bar{F}}$(cpp,L) back to the SFF, we obtain

$$F(\mathrm{cpp,L}) = \left[\frac{1}{3}\hat{J}_2T_0^{(0)} + (-1)^{J_2+J_3+1}\frac{i}{2}\hat{J}_2^2\begin{Bmatrix}1 & 1 & 1\\ J_2 & J_2 & J_3\end{Bmatrix}\times (T_1^{(1)} + T_{-1}^{(1)}) + (-1)^{J_2+J_3}\frac{\hat{J}_2^2}{4}\begin{Bmatrix}1 & 1 & 2\\ J_2 & J_2 & J_3\end{Bmatrix}(T_2^{(2)} + T_{-2}^{(2)}) + (-1)^{J_2+J_3}\frac{1}{2}\left(\frac{1}{6}\right)^{1/2}\hat{J}_2^2\begin{Bmatrix}1 & 1 & 2\\ J_2 & J_2 & J_3\end{Bmatrix}T_0^{(2)}\right]|m_2|^2 \quad (22)$$

TABLE 1: Factors $X_{q_1}^{k_1}(\mathrm{lpp},\psi,\chi)$ in the Fluorescence Intensity Function $I(\mathrm{lpp},\psi,\chi,\theta)$

	$X_{q_1}^{k_1}(\mathrm{lpp},\psi,\chi)$
X_0^0	${}^1/_9\hat{J}_1\hat{J}_2^2 + (-1)^{J_1+J_3}({}^1/_3)\hat{J}_1\hat{J}_2^4A_2A_4(3\cos^2\psi\cos^2\chi - 1)$
X_0^2	$(-1)^{J_1+J_2}({}^1/_6)({}^2/_3)^{1/2}\hat{J}_1^2\hat{J}_2^2A_1(3\cos^2\chi - 1) +$ $(-1)^{J_1+J_3+1}({}^1/_3)({}^1/_6)^{1/2}\hat{J}_1^2\hat{J}_2^4A_2A_3(3\cos^2\psi - 1) +$ $(-1)^{J_2+J_3}({}^{10}/_3)({}^1/_{14})^{1/2}\hat{J}_1^2\hat{J}_2^4A_2A_5(6\cos^2\psi\cos^2\chi -$ $3\cos^2\psi - 3\cos^2\chi + 2)$
X_1^2	$(-1)^{J_1+J_3}({}^2/_3)\hat{J}_1^2\hat{J}_2^4A_2A_3\sin\psi\cos\psi +$ $(-1)^{J_2+J_3+1}10({}^1/_{21})^{1/2}\hat{J}_1^2\hat{J}_2^4A_2A_5\sin\psi\cos\psi\,(3\cos^2\chi - 2)$
X_2^2	$(-1)^{J_1+J_2+1}({}^1/_3)\hat{J}_1^2\hat{J}_2^2A_1\sin^2\chi +$ $(-1)^{J_1+J_3+1}({}^1/_3)\hat{J}_1^2\hat{J}_2^4A_2A_3\sin^2\psi +$ $(-1)^{J_2+J_3}10({}^1/_{21})^{1/2}\hat{J}_1^2\hat{J}_2^4A_2A_5(\cos^2\psi - \cos^2\chi)$
X_0^4	$(-1)^{J_2+J_3+1}({}^1/_2)({}^5/_{14})^{1/2}\hat{J}_1^2\hat{J}_2^4A_2A_6(17\cos^2\psi\cos^2\chi -$ $5\cos^2\psi - 5\cos^2\chi + 1)$
X_1^4	$(-1)^{J_2+J_3}5({}^1/_{14})^{1/2}\hat{J}_1^2\hat{J}_2^4A_2A_6\sin\psi\cos\psi\,(5\cos^2\chi - 1)$
X_2^4	$(-1)^{J_2+J_3}5({}^1/_7)^{1/2}\hat{J}_1^2\hat{J}_2^4A_2A_6(\cos^2\psi - \cos^2\chi)$
X_3^4	$(-1)^{J_2+J_3+1}5({}^1/_2)^{1/2}\hat{J}_1^2\hat{J}_2^4A_2A_6\sin\psi\cos\psi\sin^2\chi$
X_4^4	$(-1)^{J_2+J_3}({}^5/_2)\hat{J}_1^2\hat{J}_2^4A_2A_6\sin^2\psi\sin^2\chi$

For the right circularly polarized detection mode, its fluorescence detection operator F(cpp,R) is obtained by changing the phase factor of the second term of eq 22 to $(-1)^{J_2+J_3}$. From eqs 20 and 22, it is evident that

$$F(\mathrm{cpp,L}) = \frac{1}{2}\left[F(\mathrm{unpol}) + (-1)^{J_2+J_3+1}i\hat{J}_2^2\begin{Bmatrix}1 & 1 & 1\\ J_2 & J_2 & J_3\end{Bmatrix}(T_1^{(1)} + T_{-1}^{(1)})|m_2|^2\right] \quad (23)$$

The imaginary number i in eqs 22 and 23 should be noted.

VI. Fluorescence Intensity

A. Fluorescence Intensity Functions. The fluorescence intensity is proportional to the trace of the product $\rho_e(\theta)F$, while $\rho_e(\theta)$ and F should be expanded in an identical reference frame by the same basis set of irreducible tensor operators. In the previous sections, we have carefully derived the expressions of the excited state density matrix and the fluorescence detection operators that satisfy these requirements. To derive the fluorescence intensity function, one needs the following relationship:

$$\mathrm{Tr}[T_{q_1}^{(k_1)}(bJ_2,bJ_2)^\dagger\, T_{q_2}^{(k_2)}(bJ_2,bJ_2)] = \delta_{k_1k_2}\delta_{q_1q_2} \quad (24)$$

From eqs 14, 19, and 24, we can derive the fluorescence intensity function $I(\mathrm{lpp},\psi,\chi,\theta)$ for the linearly polarized detection mode with an arbitrary polarization angle ψ

$$I(\mathrm{lpp},\psi,\chi,\theta) = \mathrm{Tr}[\rho_e(\theta)\,F(\mathrm{lpp},\psi)] = [\sum_{k_1q_1} X_{q_1}^{k_1}(\mathrm{lpp},\psi,\chi)\,{}^g\rho_{q_1}^{k_1}(\theta)]|m_1|^2|m_2|^2 \quad (25)$$

where $k_1 = 0, 2, 4$ and $q_1 \geq 0$. Because $k_1 + k_2$ is constrained to be an even, positive integer, only even rank state multipoles contribute to $I(\mathrm{lpp},\psi,\chi,\theta)$. Explicit expressions of the intensity factors $X_{q_1}^{k_1}(\mathrm{lpp},\psi,\chi)$ are listed in Table 1. When $\psi = 54.7°$ (a magic angle), the last term in eq 19 is null. The corresponding fluorescence intensity function $I(\mathrm{lpp},\psi{=}54.7°,\chi,\theta)$ is given by

$$I(\mathrm{lpp},\psi{=}54.7°,\chi,\theta) = [\sum_{\substack{k_1=0,2,4\\ q_1\geq 0}} X_{q_1}^{k_1}(\mathrm{lpp},\psi{=}54.7°,\chi)\,{}^g\rho_{q_1}^{k_1}(\theta)]|m_1|^2\,|m_2|^2 \quad (26)$$

TABLE 2: Factors $X_{q_1}^{k_1}$(lpp,ψ=54.7°,χ) in the Fluorescence Intensity Function I(lpp,ψ = 54.7°,χ,θ)

	$X_{q_1}^{k_1}$(lpp,ψ = 54.7°,χ)
X_0^0	$^1/_9\hat{J}_1\hat{J}_2^2 + (-1)^{J_1+J_3+1}(^1/_3)\hat{J}_1\hat{J}_2^4A_2A_4 \sin^2\chi$
X_0^2	$(-1)^{J_1+J_2}(^1/_6)(^2/_3)^{1/2}\hat{J}_1^2\hat{J}_2^2A_1(3\cos^2\chi - 1) +$ $(-1)^{J_2+J_3}(^5/_3)(^2/_7)^{1/2}\hat{J}_1^2\hat{J}_2^4A_2A_5 \sin^2\chi$
X_1^2	$(-1)^{J_1+J_3}(^2/_9)(2)^{1/2}\hat{J}_1^2\hat{J}_2^4A_2A_3 +$ $(-1)^{J_2+J_3+1}(^{10}/_3)(^2/_{21})^{1/2}\hat{J}_1^2\hat{J}_2^4A_2A_5(3\cos^2\chi - 2)$
X_2^2	$(-1)^{J_1+J_3+1}(^2/_9)\hat{J}_1^2\hat{J}_2^4A_2A_3 + (-1)^{J_1+J_2+1}(^1/_3)\hat{J}_1^2\hat{J}_2^2A_1 \sin^2\chi +$ $(-1)^{J_2+J_3+1}(^{10}/_3)(^1/_{21})^{1/2}\hat{J}_1^2\hat{J}_2^4A_2A_5(3\cos^2\chi - 1)$
X_0^4	$(-1)^{J_2+J_3}(^1/_3)(^5/_{14})^{1/2}\hat{J}_1^2\hat{J}_2^4A_2A_6 \sin^2\chi$
X_1^4	$(-1)^{J_2+J_3}(^5/_3)(^1/_7)^{1/2}\hat{J}_1^2\hat{J}_2^4A_2A_6(5\cos^2\chi - 1)$
X_2^4	$(-1)^{J_2+J_3+1}(^5/_3)(^1/_7)^{1/2}\hat{J}_1^2\hat{J}_2^4A_2A_6(3\cos^2\chi - 1)$
X_3^4	$(-1)^{J_2+J_3+1}(^5/_3)\hat{J}_1^2\hat{J}_2^4A_2A_6 \sin^2\chi$
X_4^4	$(-1)^{J_2+J_3}(^5/_3)\hat{J}_1^2\hat{J}_2^4A_2A_6 \sin^2\chi$

TABLE 3: Factors $X_{q_1}^{k_1}$(unpol,χ) in the Fluorescence Intensity Function I(unpol,χ,θ)

	$X_{q_1}^{k_1}$(unpol,χ)
X_0^0	$^2/_9\hat{J}_1\hat{J}_2^2 + (-1)^{J_1+J_3}(^1/_6)\hat{J}_1\hat{J}_2^4A_2A_4(3\cos 2\chi - 1)$
X_0^2	$(-1)^{J_1+J_3+1}(^1/_3)(^1/_6)^{1/2}\hat{J}_1^2\hat{J}_2^4A_2A_3 +$ $(-)^{J_2+J_3}(^{10}/_3)(^1/_{14})^{1/2}\hat{J}_1^2\hat{J}_2^4A_2A_5 +$ $(-1)^{J_1+J_2}(^1/_3)(^2/_3)^{1/2}\hat{J}_1^2\hat{J}_2^2A_1(3\cos^2\chi - 1)$
X_2^2	$(-1)^{J_1+J_3+1}(^1/_3)\hat{J}_2^2\hat{J}_2^4A_2A_3 +$ $(-1)^{J_1+J_3+1}(^2/_3)\hat{J}_1^2\hat{J}_2^2A_1 \sin^2\chi +$ $(-1)^{J_2+J_3+1}10(^1/_{21})^{1/2}\hat{J}_1^2\hat{J}_2^4A_2A_5(2\cos^2\chi - 1)$
X_0^4	$(-1)^{J_2+J_3+1}(^1/_2)(^5/_{14})^{1/2}\hat{J}_1^2\hat{J}_2^4A_2A_6(7\cos^2\chi - 3)$
X_2^4	$(-1)^{J_2+J_3+1}5(^1/_7)^{1/2}\hat{J}_1^2\hat{J}_2^4A_2A_6(2\cos^2\chi - 1)$
X_4^4	$(-1)^{J_2+J_3}(^5/_2)\hat{J}_1^2\hat{J}_2^4A_2A_6 \sin^2\chi$

where explicit expressions of the intensity factors $X_{q_1}^{k_1}$(lpp,ψ=54.7°,χ) are listed in Table 2. Examining the χ-dependence of these intensity factors in Table 2, we realize that various $X_{q_1}^{k_1}$ are linear combinations of 1 and $\cos^2\chi$. It implies that only intensity measurements at two different probe angles χ for a chosen polarization angle ψ are linearly independent; in addition, all the measurements at other probe angles are redundant and can improve solely the accuracy of the determination of ${}^g\rho_{q_1}^{k_1}(\theta)$.

For an unpolarized detection mode, the fluorescence intensity function I(unpol,χ,θ) can be obtained from eqs 14, 20, and 24

$$I(\text{unpol},\chi,\theta) = [\sum_{k_1q_1} X_{q_1}^{k_1}(\text{unpol},\chi,\theta)\ {}^g\rho_{q_1}^{k_1}(\theta)]|m_1|^2\ |m_2|^2 \quad (27)$$

where $k_1 = 0$, 2, 4, and odd components are absent. In Table 3, we list the explicit expressions of the intensity factors $X_{q_1}^{k_1}$(unpol,χ,θ) for the image simulations.

Similarly, we can cast the fluorescence intensity function for the circularly polarized detection mode into the following form:

$$I(\text{cpp,L},\chi,\theta) = \text{Tr}[\rho_e(\theta)\ F(\text{cpp,L})] = \frac{1}{2}I(\text{unpol},\chi,\theta) + [\sum_{k_1q_1} X_{q_1}^{k_1}(\text{cpp,L},\chi)\ {}^g\rho_{q_1}^{k_1}(\theta)]|m_1|^2\ |m_2|^2 \quad (28)$$

where $k_1 = 1$, 3 and even components are absent. In other words, ${}^g\rho_1^1(\theta)$, ${}^g\rho_1^3(\theta)$, and ${}^g\rho_3^3(\theta)$ can be determined in a circularly polarized detection mode, while the orientation parameter ${}^g\rho_2^3(\theta)$ is excluded. Explicit expressions of $X_{q_1}^{k_1}$(cpp,L,χ) are listed in Table 4, and I(unpol,χ,θ) in the above equation is given in eq 27. Various 6-j and 9-j symbols which are abbreviated by the notations A_n in Tables 1−4 are defined explicitly in Table 5.

TABLE 4: Factors $X_{q_1}^{k_1}$(cpp,L,χ) in the Fluorescence Intensity Function I(cpp,L,χ,θ)

	$X_{q_1}^{k_1}$(cpp,L,χ)
X_1^1	$(-1)^{J_1+J_3+1}(^1/_3)\hat{J}_1^2\hat{J}_2^4A_7A_8 +$ $(-1)^{J_2+J_3+1}(^1/_2)\hat{J}_1^2\hat{J}_2^4A_7A_9(1 - 3\cos 2\chi)$
X_1^3	$(-1)^{J_2+J_3+1}(^1/_2)\hat{J}_1^2\hat{J}_2^2A_7A_{10}(3 - 7\cos^2\chi)$
X_3^3	$(-1)^{J_2+J_3+1}(^1/_2)(15)^{1/2}\hat{J}_1^2\hat{J}_2^4A_7A_{10} \sin^2\chi$

TABLE 5: Explicit Forms of A_n

$$A_1 = \begin{Bmatrix} 1 & 1 & 2 \\ J_1 & J_1 & J_2 \end{Bmatrix} \quad A_2 = \begin{Bmatrix} 1 & 1 & 2 \\ J_2 & J_2 & J_3 \end{Bmatrix} \quad A_3 = \begin{Bmatrix} J_1 & J_1 & 2 \\ J_2 & J_2 & 1 \end{Bmatrix}$$

$$A_4 = \begin{Bmatrix} 1 & 1 & 2 \\ J_2 & J_2 & J_1 \end{Bmatrix} \quad A_5 = \begin{Bmatrix} 2 & 2 & 2 \\ J_1 & J_2 & 1 \\ J_1 & J_2 & 1 \end{Bmatrix} \quad A_6 = \begin{Bmatrix} 4 & 2 & 2 \\ J_1 & J_2 & 1 \\ J_1 & J_2 & 1 \end{Bmatrix}$$

$$A_7 = \begin{Bmatrix} 1 & 1 & 1 \\ J_2 & J_2 & J_3 \end{Bmatrix} \quad A_8 = \begin{Bmatrix} J_1 & J_1 & 1 \\ J_2 & J_2 & 1 \end{Bmatrix} \quad A_9 = \begin{Bmatrix} 1 & 1 & 2 \\ J_1 & J_2 & 1 \\ J_1 & J_2 & 1 \end{Bmatrix}$$

$$A_{10} = \begin{Bmatrix} 3 & 1 & 2 \\ J_1 & J_2 & 1 \\ J_1 & J_2 & 1 \end{Bmatrix}$$

B. Intensity Factors and Practical Considerations. The relative contributions of intensity factors in the fluorescence intensity function open a question of how accurately one can determine the various state multipoles. To assess their contributions, we have programmed the intensity factors $X_{q_1}^{k_1}$(lpp,ψ = 54.7°,χ) in Table 2 and calculated their numerical values as functions of the probe angle χ and transition sequences. A few representative results are depicted in Figures 5 and 6. The patterns of the intensity factors as functions of the probe angle χ resemble one another for a selected ΔJ transition sequence ($J_1 \rightarrow J_2 \rightarrow J_3$), no matter whether the quantum number J_1 is small or large. Examining Figures 5 and 6, we notice that $X_{q_1}^4$'s contribute relatively less than their corresponding $X_{q_1}^2$'s do, except in the case of the transition $J_1 \rightarrow J_2 \rightarrow J_3 = (2 \rightarrow 1 \rightarrow 0)$. Judging from the relative contributions and functional dependences on the probe angle χ of the intensity factors $X_{q_1}^4$, we anticipate that the experimental determination of the alignment parameters (${}^g\rho_{q_1}^4(\theta)$) will be difficult, especially for internal states with large J_1. Similarly, we have calculated numerical values of $X_{q_1}^{k_1}$(cpp,L,χ) in Table 4 as functions of the probe angle χ and transition sequences. Prototypical results are presented in Figures 7 and 8.

The observed image patterns in a fluorescence-imaging experiment depend on other parameters, that is, the collection efficiency of the 2D imaging detector, the laser energies, the Franck−Condon factors, and the angular distribution function $N(\theta)$. As an example, the experimentally measured $X_{q_1}^{k_1}$(lpp,ψ=54.7°,χ,θ) should be given by

$$I_{\text{exp}}(\text{lpp},\psi{=}54.7°,\chi,\theta) = c[\sum_{k_1q_1} X_{q_1}^{k_1}(\text{lpp},\psi{=}54.7°,\chi)\ {}^g\rho_{q_1}^{k_1}(\theta)]|m_1|^2|m_2|^2N(\theta) \quad (29)$$

where c is a proportionality constant.

In the case of the linearly polarized detection mode, we can set up a simultaneous equation of ${}^g\rho_{q_1}^{k_1}(\theta)$ by measuring I(lpp,ψ_1,χ_1,θ) and I(lpp,ψ_1,χ_2,θ) for a chosen polarization angle ψ_1, where χ_1 and $\chi_2 \neq 0°$ or 90°. These two measurements can be normalized by the experimentally measured pattern at χ = 0°. Thus, we have

$$\frac{\sum_{k_1 q_1} X_{q_1}^{k_1}(\mathrm{lpp},\psi_1,\chi_i)\ {}^{\mathrm{g}}\rho_{q_1}^{k_1}(\theta)}{\sum_{k_1 q_1} X_{q_1}^{k_1}(\mathrm{lpp},\psi_1,\chi{=}0°)\ {}^{\mathrm{g}}\rho_{q_1}^{k_1}(\theta)} = \frac{I_{\mathrm{exp}}(\mathrm{lpp},\psi_1,\chi_i,\theta)}{I_{\mathrm{exp}}(\mathrm{lpp},\psi_1,\chi{=}0°,\theta)} \quad (30)$$

where $\chi_i = \chi_1$ or χ_2 and unknown parameters can be eliminated. From four different selections of the polarization angle ψ ($\psi \neq 0°$ or 90°), we can obtain eight linearly independent equations of ${}^{\mathrm{g}}\rho_{q_1}^{k_1}(\theta)$ ($k_1 = 0$, 2, 4). From the normalization condition on $\rho_{\mathrm{g}}(\theta)$, that is, $\mathrm{Tr}\rho_{\mathrm{g}}(\theta) = 1$, it follows that[40]

$${}^{\mathrm{g}}\rho_0^0(\theta) = \hat{J}_1^{-1} \quad (31)$$

for a sharply defined J_1 state. Thus, we have enough inputs for an absolute determination of the nine population and alignment parameters of the selected internal state along various scattering angles from 12 independent measurements. Additional measurements at other polarization angles and transition sequences can be employed to improve the accuracy of the calculation.

In the case of the unpolarized detection mode, we can only determine six state multipoles of even components, that is, ${}^{\mathrm{g}}\rho_0^0(\theta)$, ${}^{\mathrm{g}}\rho_0^2(\theta)$, ${}^{\mathrm{g}}\rho_2^2(\theta)$, ${}^{\mathrm{g}}\rho_0^4(\theta)$, ${}^{\mathrm{g}}\rho_2^4(\theta)$, and ${}^{\mathrm{g}}\rho_4^4(\theta)$. Excluding eq 31, we need five linearly independent equations of state multipoles. For transitions with three rotational branches ($\Sigma - \Pi$), we can set up a simultaneous equation to determine these six state multipoles by tuning the probe laser frequencies to various resonances. For transitions with only two rotational branches ($\Sigma - \Sigma$, $\Pi - \Pi$), we have to resort to the scheme of the linearly polarized detection mode.

In the case of the circularly polarized detection mode, we have the opportunity to determine orientation parameters, ${}^{\mathrm{g}}\rho_1^1(\theta)$, ${}^{\mathrm{g}}\rho_1^3(\theta)$, and ${}^{\mathrm{g}}\rho_3^3(\theta)$, provided that even rank state multipoles have been known beforehand. In principle, three linearly independent equations of ${}^{\mathrm{g}}\rho_1^1(\theta)$, ${}^{\mathrm{g}}\rho_1^3(\theta)$, and ${}^{\mathrm{g}}\rho_3^3(\theta)$ can be found easily by selecting two different probe angles χ and tuning the probe laser to various rotational branches.

VII. Fluorescence Image Patterns and v−J Correlations

To illustrate the application of the present formalism, it is interesting to simulate the fluorescence image patterns of a system with known state multipoles. For simplicity, we consider a photofragmentation process so that photofragments A exhibit only **v**−**J** correlation; that is, the angular momentum polarization has no explicit dependence on the scattering angle θ. Two limiting cases of **v**−**J** correlations are considered: photofragments with a cartwheel motion (**v** ⊥ **J**) and photofragments with a helicopter motion (**v** ∥ **J**). In the language of density matrices, the non-null matrix element for the cartwheel motion is $\rho_{MM'} \equiv |JM\rangle\langle JM'| = |J0\rangle\langle J0|$, where the projection of angular momentum vector onto the quantization axis is null. In a reference frame defined with its Z'-axis along the recoil direction, the density matrix of photofragments in a ground electronic state is $\rho_{\mathrm{g}}(\mathrm{cw}) = |J_1 0\rangle\langle J_1 0|$, where cw denotes the cartwheel motion and J_1 is a rotational angular momentum quantum number. Similarly, the non-null matrix elements for a helicopter motion should be $\rho_{J_1 J_1} = {}^1/_2$ and $\rho_{-J_1 -J_1} = {}^1/_2$. Its density matrix is given by $\rho_{\mathrm{g}}(\mathrm{hc}) = {}^1/_2[|J_1 J_1\rangle\langle J_1 J_1| + |J_1 - J_1\rangle\langle J_1 - J_1|]$, where hc denotes the helicopter motion. The choice of $\rho_{\mathrm{g}}(\mathrm{hc}) = |J_1 J_1\rangle\langle J_1 J_1|$ or $|J_1 - J_1\rangle\langle J_1 - J_1|$ is unacceptable for the helicoper motion, due to the fact that neither of them satisfies the reflection invariance of the density matrix in the scattering plane.[40] The ground state density matrix can be expanded in terms of the irreducible tensor operator $\tilde{T}_{q_1}^{(k_1)}(aJ_1,aJ_1)$

$$\rho_{\mathrm{g}}(\mathrm{cw}) = \sum_{k_1} (-1)^{J_1} \hat{k}_1 \begin{pmatrix} J_1 & J_1 & k_1 \\ 0 & 0 & 0 \end{pmatrix} \tilde{T}_0^{(k_1)}(aJ_1,aJ_1) \quad (32)$$

and

$$\rho_{\mathrm{g}}(\mathrm{hc}) = \sum_{k_1} \hat{k}_1 \begin{pmatrix} J_1 & J_1 & k_1 \\ J_1 & -J_1 & 0 \end{pmatrix} \tilde{T}_0^{(k_1)}(aJ_1,aJ_1) \quad (33)$$

where k_1 is an even, positive integer for both cases. From the transformation properties of the irreducible tensor operators, we have

$$\rho_{\mathrm{g}}(\mathrm{cw}) = \sum_{k_1 q_1} (-1)^{J_1} \hat{k}_1 \begin{pmatrix} J_1 & J_1 & k_1 \\ 0 & 0 & 0 \end{pmatrix} d_{q_1 0}^{k_1}(\theta)\ T_{q_1}^{(k_1)}(aJ_1,aJ_1)$$

$$= \sum_{k_1 q_1} {}^{\mathrm{g}}\rho_{q_1}^{k_1}(\mathrm{cw},\theta)\ T_{q_1}^{(k_1)}(aJ_1,aJ_1) \quad (34)$$

and

$$\rho_{\mathrm{g}}(\mathrm{hc}) = \sum_{k_1 q_1} \hat{k}_1 \begin{pmatrix} J_1 & J_1 & k_1 \\ J_1 & -J_1 & 0 \end{pmatrix} d_{q_1 0}^{k_1}(\theta)\ T_{q_1}^{(k_1)}(aJ_1,aJ_1)$$

$$= \sum_{k_1 q_1} {}^{\mathrm{g}}\rho_{q_1}^{k_1}(\mathrm{hc},\theta)\ T_{q_1}^{(k_1)}(aJ_1,aJ_1) \quad (35)$$

where $T_{q_1}^{(k_1)}(aJ_1,aJ_1)$ is defined in the SFF. ${}^{\mathrm{g}}\rho_{q_1}^{k_1}(\mathrm{cw},\theta)$ and ${}^{\mathrm{g}}\rho_{q_1}^{k_1}(\mathrm{hc},\theta)$ are the state multipoles for the cartwheel and the helicopter motion of photofragments, respectively. As soon as we obtain the explicit forms of these state multipoles, we can utilize the fluorescence intensity function in section VI to calculate the fluorescence image patterns as functions of experimental parameters.

For later developments, we first clarify the spectroscopic terminology utilized in this work. In the numerical calculations, we consider photofragments with the initial K_1 quantum number to be 0 or ±1. This limitation corresponds to a consideration of the Σ or Π electronic state of a diatomic photofragment. A parallel or a perpendicular transition denotes the selection rule on K to be $\Delta K = 0$ or ±1. Transitions of the P, Q, and R branches represent their ΔJ selection rule to be −1, 0, and +1, respectively. Only P and R branches are allowed for a parallel transition from $K_1 = 0$. We assume that spectroscopically unresolved emissions are monitored such that a sum of fluorescence intensities over the allowed P, Q, and R branches should be executed in the calculation. Further, it is assumed that the parallel or perpendicular characteristics of the absorption process is preserved in the emission. For example, a parallel transition from the $K_1 = 0$ level ends up in a $K_2 = 0$ state. In the emission, only the $K_3 = 0$ state is allowed to account for the preservation of the $\Delta K = 0$ selection rule.

It should be reminded that only population ($k_1 = 0$) and alignment parameters ($k_1 = 2$, 4) contribute to the fluorescence intensity as long as linearly polarized fluorescence photons are monitored in the present excitation scheme. For reference, the numerical values of ${}^{\mathrm{g}}\rho_0^{k_1}(\mathrm{cw})$ and ${}^{\mathrm{g}}\rho_0^{k_1}(\mathrm{hc})$ in the recoil frame for $k_1 = 0$, 2, and 4 are listed in Table 6, in which both a low-J ($J_1 = 2$) and a high-J ($J_1 = 20$) case are considered. According to eq 27 and Table 6, we have calculated $I(\mathrm{unpol},\chi,\theta)$ as functions of experimental parameters. These simulated fluorescence patterns are depicted in Figures 9 and 10, in which the following selections have been made: (1) the initial $K_1 = 0$, (2) a perpendicular transition is considered, and (3) the rotational angular momentum $J_1 = 2$ or 20. From Figures 9

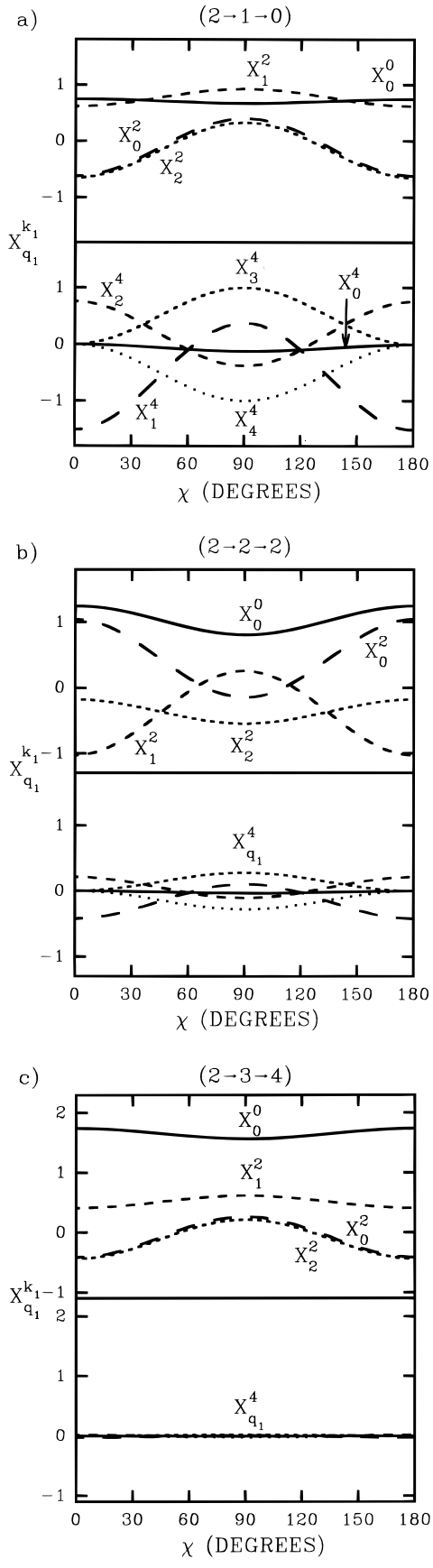

Figure 5. Plots of $X^{k_1}_{q_1}$(lpp,$\psi = 54.7°$,χ)versus probe angle χ: (a) ($J_1 \rightarrow J_2 \rightarrow J_3$) = (2 → 1 → 0); (b) ($J_1 \rightarrow J_2 \rightarrow J_3$) = (2 → 2 → 2); (c) ($J_1 \rightarrow J_2 \rightarrow J_3$) = (2 → 3 → 4).

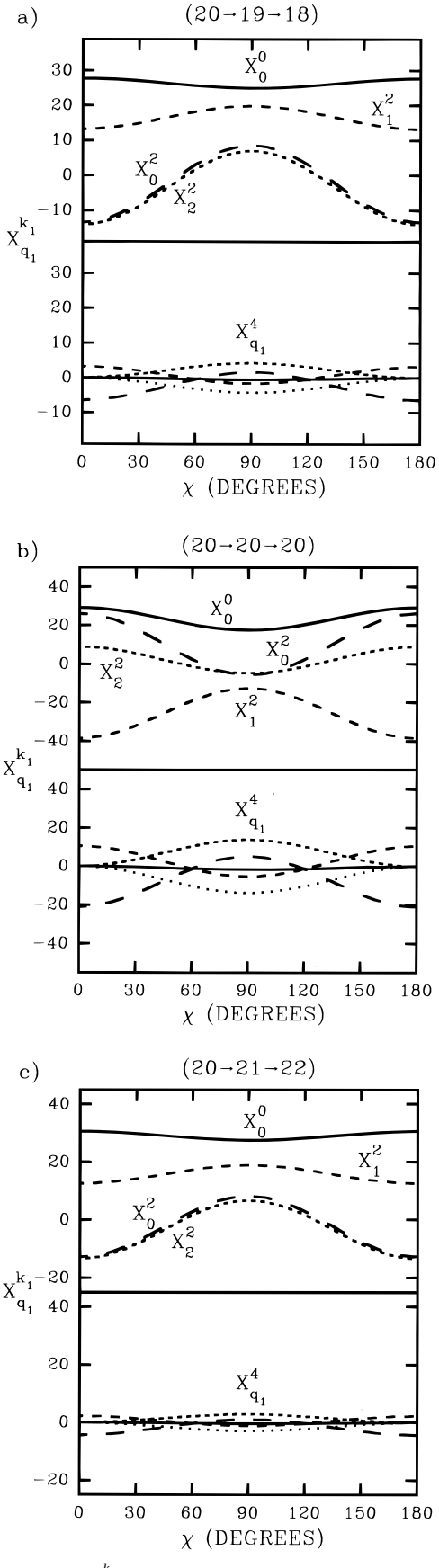

Figure 6. Plots of $X^{k_1}_{q_1}$(lpp,$\psi = 54.7°$,χ) versus probe angle χ: (a) ($J_1 \rightarrow J_2 \rightarrow J_3$) = (20 → 19 → 18); (b) ($J_1 \rightarrow J_2 \rightarrow J_3$) = (20 → 20 → 20); (c) ($J_1 \rightarrow J_2 \rightarrow J_3$) = (20 → 21 → 22).

and 10, distinctive differences between fluorescence intensity functions for $\mathbf{v} \parallel \mathbf{J}$ and $\mathbf{v} \perp \mathbf{J}$ of the same rotational branch are the major feature. For photofragments with the same $\mathbf{v}-\mathbf{J}$ correlation, the different behavior of I(unpol,χ,θ) under the P and R branches in comparison with those under the Q branch is another feature. When $J_1 = 20$, the behavior of I(unpol,χ,θ) approaches that predicted by the classical picture of dipole transition.[41]

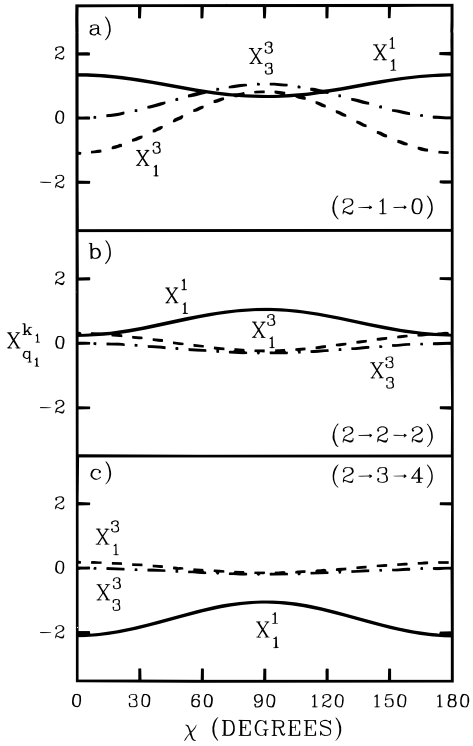

Figure 7. Plots of $X^{k_1}_{q_1}$(cpp,L,χ) versus probe angle χ: (a) ($J_1 \rightarrow J_2 \rightarrow J_3$) = (2 → 1 → 0); (b) ($J_1 \rightarrow J_2 \rightarrow J_3$) = (2 → 2 → 2); (c) ($J_1 \rightarrow J_2 \rightarrow J_3$) = (2 → 3 → 4).

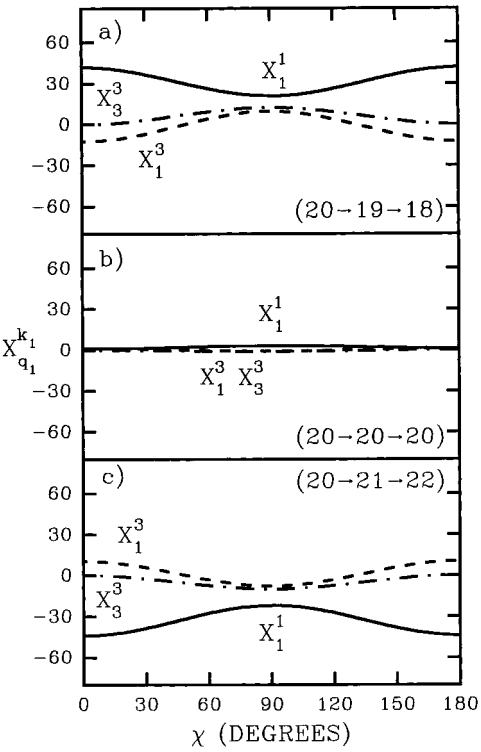

Figure 8. Plots of $X^{k_1}_{q_1}$(cpp,L,χ) versus probe angle χ: (a) ($J_1 \rightarrow J_2 \rightarrow J_3$) = (20 → 19 → 18); (b) ($J_1 \rightarrow J_2 \rightarrow J_3$) = (20 → 20 → 20); (c) ($J_1 \rightarrow J_2 \rightarrow J_3$) = (20 → 21 → 22).

For a parallel transition from the $K_1 = 0$ level, the fluorescence pattern under the Q branch should be deleted. Regarding the behavior of fluorescence patterns under the P and R branches, we have found by numerical calculations that fluorescence patterns for the parallel transition are almost identical to those reported in Figures 9 and 10. We have also calculated fluorescence patterns from the $K_1 = 1$ level for both the parallel and the perpendicular transitions. Those simulated

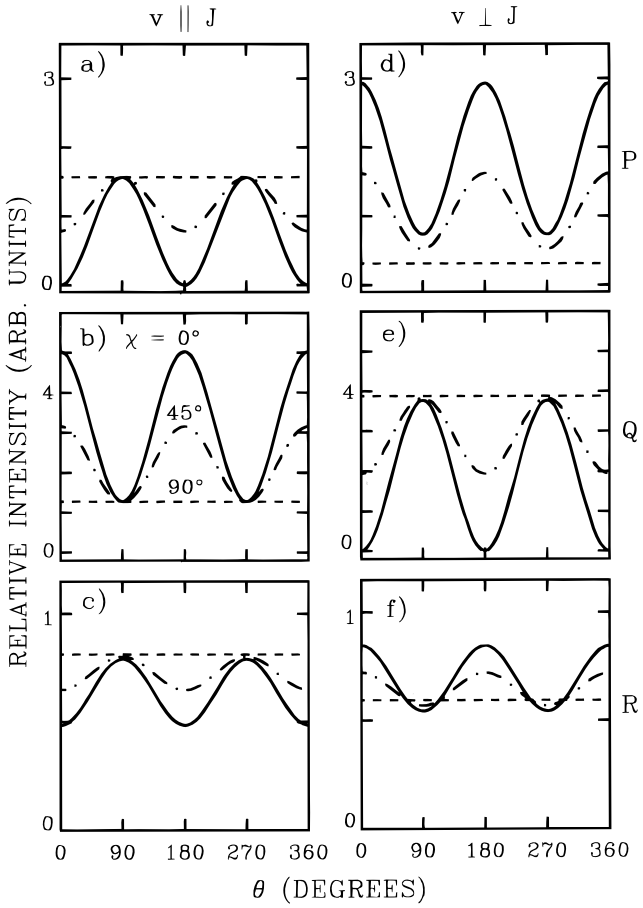

Figure 9. Plots of simulated I(unpol,χ,θ) for $J_1 = 2$ versus scattering angle θ. Frames a, b, and c are for the case of **v** || **J**. Frames d, e, and f are for the case of **v** ⊥ **J**. The ΔJ selection rule (rotational branch) of each row is marked by P, Q, or R on the right margin. As an example, frames b and e have $\Delta J = 0$ (Q branch). For clarity, plots of I(unpol,χ,θ) for $\chi = 0°$ (—), 45° (—•—), and 90° (- - -) are presented.

TABLE 6: Numerical Values of State Multipoles

state multipole		**v** ⊥ **J**	**v** || **J**
${}^{g}\rho_0^{k_1}(J_1{=}2)$	$k_1 = 0$	0.447 21	0.447 21
	$k_1 = 2$	−0.534 52	0.534 52
	$k_1 = 4$	0.717 14	0.119 52
${}^{g}\rho_0^{k_1}(J_1{=}20)$	$k_1 = 0$	0.156 17	0.156 17
	$k_1 = 2$	−0.174 76	0.324 56
	$k_1 = 4$	0.176 22	0.366 94

fluorescence patterns are quite similar to the corresponding frames in Figures 9 and 10.

To visualize the simulated image patterns, we have combined prototypical results in Figure 10 ($J_1 = 20$, $\chi = 0°$) with the angular distribution function $N(\theta) = (4\pi)^{-1}[1 + \beta P_2(\cos\theta)]$, where P_2 is a second-order Legendre polynomial and the anisotropy parameter β is chosen to be 0 (isotropic), 2 (cosine-squared), and −1 (sine-squared). A Gaussian velocity spread of photofragments has been implemented in the computer program such that the fluorescence images are easily discernible. In Figure 11, we reproduce these simulated fluorescence image frames. A unique correspondence between image patterns and physical observables can be established. This pattern recognition is useful to identify **v**−**J** correlations by visual inspection. Focusing on the same issue, Siebbeles et al.,[46] Cline and co-workers,[47] and Suzuki and co-workers[48] have advanced our knowledge on **k′**−**J′** correlations from both theoretical treatments and experimental studies.

VIII. Discussion

In section III, the propagation direction of the probe laser sheet is chosen to be along the X-axis of the SFF. As a matter

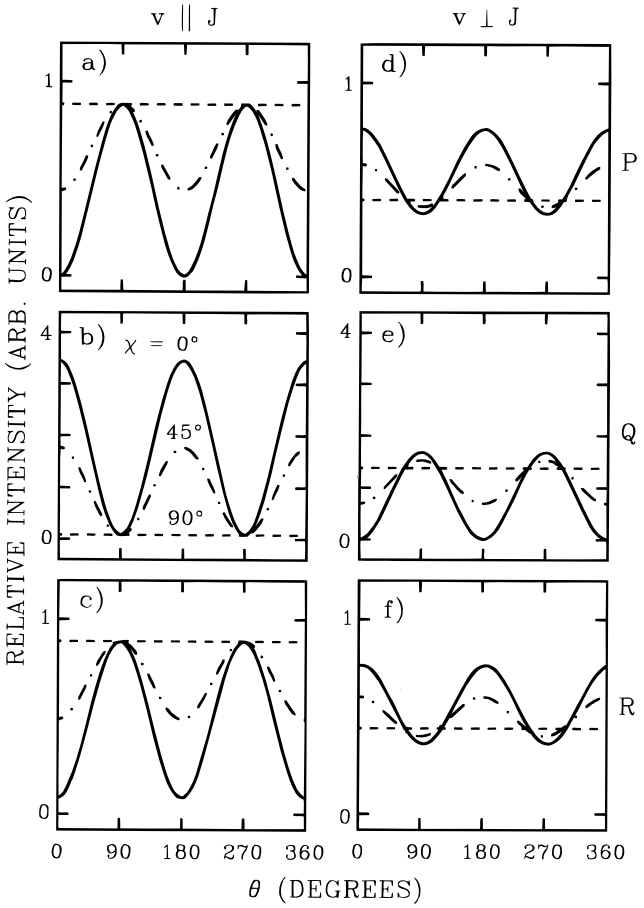

Figure 10. Plots of simulated $I(\text{unpol},\chi,\theta)$ for $J_1 = 20$ versus scattering angle θ. See the figure caption of Figure 9 for a detailed description.

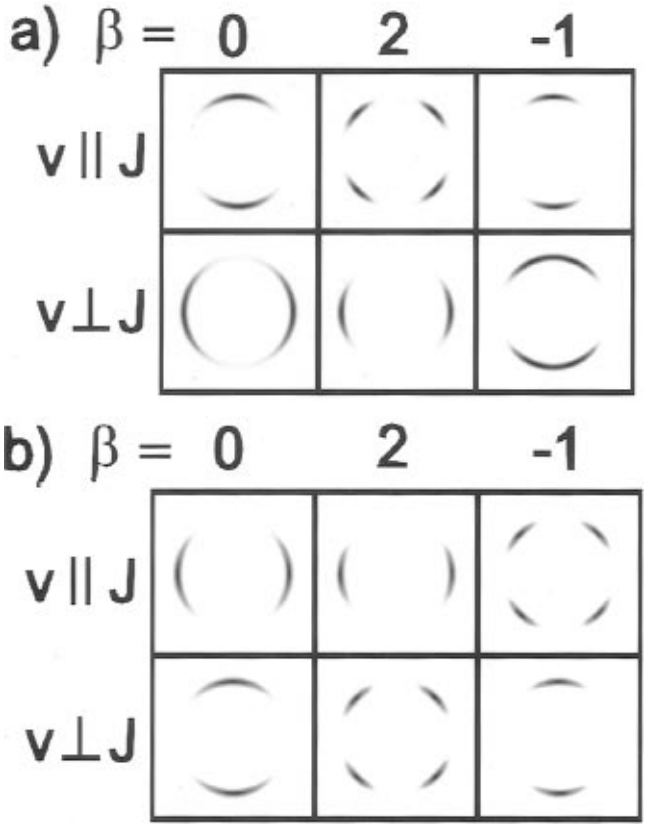

Figure 11. Simulated image patterns of photofragments for the case of $J_1 = 20$ and probe angle $\chi = 0°$: (a) P branch; (b) Q branch. To read these images, each row corresponds to a specific motion ($\mathbf{v} \parallel \mathbf{J}$ or $\mathbf{v} \perp \mathbf{J}$), and each column is for a chosen anisotropy parameter β (0, 2, or -1). Each image is oriented such that the Z-axis of the SFF lies horizontally in the plane of the figure and bisects the square that surrounds the image. Fluorescence intensities of each image frame have been normalized to the same scale. See Figure 10 for information on relative intensities.

of fact, this choice is quite flexible, as long as the plane defined by the polarization direction of the photolysis laser and the moving direction of the precursors is sliced. In other words, identical information of state multipoles can be obtained in various experimental configurations, provided that the propagation direction of the probe laser is rotated in the $X-Z$-plane.

To compare the experimentally measured state multipoles with the bipolar moments in the formalism of Dixon,[12] the first step is to transform the reference frame from the SFF to the recoil frame. From previous results, we have $\rho_g = \sum_{k_1 q_1 q_2} {}^g\rho_{q_1}^{k_1}(\theta)\, d_{q_1 q_2}^{k_1}(\theta)\, \underline{T}_{q_2}^{(k_1)}(aJ_1,aJ_1)$, where $\underline{T}_{q_2}^{(k_1)}(aJ_1,aJ_1)$ is defined in the recoil frame along the scattering angle θ. Because $\underline{T}_{q_2}^{(k_1)\dagger}$ can be expressed as a linear combination of bipolar harmonics employed by Dixon,[12] one can find the correspondence between state multipoles and bipolar moments by taking the trace of $\rho_g \underline{T}_{q_2}^{(k_1)\dagger}$. We will not proceed further on this subject in the present report.

If the Newton sphere of products is uniformly excited by a linearly polarized probe laser beam, we can sum contributions from successive layers to obtain the Doppler profile function $D(\nu,\chi)$ in a typical Doppler spectroscopic measurement.[49] For example, the Doppler profile function in an unpolarized detection mode under the condition of the proposed excitation geometry can be proven to be

$$D(\nu,\chi) = \int v^2 \sin\theta \Big[\sum_{k_1 q_1 q_2} X_{q_2}^{k_1}(\text{unpol},\chi) \times D_{q_2 q_1}^{k_1}(\phi,\theta,0)\, {}^g\rho_{q_1}^{k_1}(\theta) \Big] |m_1|^2 |m_2|^2 N(\theta)\, f(v) \times \delta\left[\nu - \nu_0\left(1 + \frac{v}{c}\sin\theta\cos\phi\right)\right] dv\, d\theta\, d\phi \quad (36)$$

where $f(v)$ is a velocity distribution function, ν_0 is the unshifted resonance frequency, and ν is the probe laser frequency. ${}^g\rho_{q_1}^{k_1}(\theta)$ in the above equation is defined in the recoil frame. In the presence of $\mathbf{k}'-\mathbf{J}'$ correlations, these state multipoles have explicit dependences on the scattering angle θ. Therefore, the Radon transform[50] in eq 36 will mix every term in the integrand together. $D(\nu,\chi)$ cannot be expressed as a linear combination of ${}^g\rho_{q_1}^{k_1}(\theta)$. Thus, the correlation of angular momentum polarizations with the recoil directions is either scrambled or averaged out in any projection experiment, unless reaction products exhibit only $\mathbf{v}-\mathbf{J}$ correlations and display no $\mathbf{k}'-\mathbf{J}'$ correlations. On the other hand, the proposed detection scheme can measure state multipoles without a priori knowledge on $N(\theta)$ and $f(v)$. We conclude that the proposed detection scheme which employs fluorescence-imaging techniques has advantages over the conventional projection experiments.

For reaction products with high recoil velocities, their Doppler shifts can exceed the bandwidth of the probe laser. Under the circumstances, one should tune the probe laser frequencies across the whole range of the Doppler width and sum the resultant image frames before analyzing the fluorescence image patterns.

It is difficult to compare the present formalism with previous treatments, for example, the theoretical framework developed by Kummel, Sitz, and Zare.[18] Kummel et al. employed the tensor contraction method and chose the alignment as well as the orientation moments to be real. In our analysis, the only constraint on the state multipoles is the reflection invariance of the density matrix in the scattering plane (see eqs 3 and 4). Thus, alignment and orientation moments in the work by Kummel et al.[18] must be a linear combination of the state

multipoles in the present formalism. These two formalisms should be equivalent. We also noted that symmetry-adapted differential cross sections have been utilized in a recent publication by Zare and co-workers.[31] In our framework, there are three criteria to judge the validity of the fluorescence intensity function; they are: (1) the fluorescence intensity function should be real; (2) simulated fluorescence intensities cannot be negative; (3) simulated fluorescence image patterns with **v**−**J** correlations should be consistent with the classical picture of dipole transitions when J_1 is large. These criteria are met in every respect. To explore the experimental advantage of an elliptically polarized excitation scheme, we have studied this alternative method in detail and will publish it elsewhere.

IX. Conclusions

We have proposed a fluorescence imaging experiment to determine state multipoles of the density matrix of reaction products along various recoil directions **k′**. Information on **k′**−**J′** correlations of reaction products can be obtained by monitoring the intensity variations of the image patterns as a function of the probe angles χ and transition sequences.

From detailed analyses of the 1 + 1 LIF detection scheme, we have shown that population (${}^{g}\rho_0^0(\theta)$) and alignment parameters (${}^{g}\rho_0^2(\theta)$, ${}^{g}\rho_1^2(\theta)$, ${}^{g}\rho_2^2(\theta)$, ${}^{g}\rho_0^4(\theta)$, ${}^{g}\rho_1^4(\theta)$, ${}^{g}\rho_2^4(\theta)$, ${}^{g}\rho_3^4(\theta)$, ${}^{g}\rho_4^4(\theta)$) of reaction products in a specific quantum state can be uniquely determined experimentally. For the present detection scheme in which the probe laser sheet is linearly polarized, orientation parameters (${}^{g}\rho_1^1(\theta)$, ${}^{g}\rho_1^3(\theta)$, ${}^{g}\rho_3^3(\theta)$) of reaction products can be determined by monitoring circularly polarized fluorescence photons. Fluorescence intensity functions of the image patterns are given explicitly as functions of the probe angle χ and angular momentum quantum numbers in the transition sequence. A simulation study has been implemented to establish a pattern recognition of fluorescence images of photofragments with **v**−**J** correlation. We expect that the study of **k′**−**J′** correlations of reaction products should lead to new information on the anisotropy of potential energy surfaces of reactive systems.

Acknowledgment. This research was supported by the National Science Council of the Republic of China.

References and Notes

(1) Simons, J. P. *J. Phys. Chem.* **1987**, *91*, 5378.
(2) Houston, P. L. *J. Phys. Chem.* **1987**, *91*, 5388.
(3) Orr-Ewing, A. J.; Zare, R. N. *Annu. Rev. Phys. Chem.* **1994**, *45*, 315.
(4) Case, D. A.; Herschbach, D. R. *Mol. Phys.* **1975**, *30*, 1537.
(5) Case, D. A.; Herschbach, D. R. *J. Chem. Phys.* **1976**, *64*, 4212.
(6) Case, D. A.; McClelland, G. M.; Herschbach, D. R. *Mol. Phys.* **1978**, *35*, 541.
(7) Zare, R. N.; Herschbach, D. R. *Proc. IEEE* **1963**, *51*, 173.
(8) Hall, G. E.; Sivakumar, N.; Houston, P. L.; Burak, I. *Phys. Rev. Lett.* **1986**, *56*, 1671.
(9) Dubs, M; Brühlmann, U.; Huber, J. R. *J. Chem. Phys.* **1986**, *84*, 3106.
(10) Gericke, K.-H.; Klee, S.; Comes, F. J.; Dixon, R. N. *J. Chem. Phys.* **1986**, *85*, 4463.
(11) Docker, M. P.; Hodgson, A.; Simons, J. P. *Chem. Phys. Lett.* **1986**, *128*, 264.
(12) Dixon, R. N. *J. Chem. Phys.* **1986**, *85*, 1866.
(13) Hall, G. E.; Sivakumar, N.; Chawla, D.; Houston, P. L.; Burak, I. *J. Chem. Phys.* **1988**, *88*, 3682.
(14) Greene, C. H.; Zare, R. N. *J. Chem. Phys.* **1983**, *78*, 6741.
(15) Jacobs, D. C.; Zare, R. N. *J. Chem. Phys.* **1986**, *85*, 5457.
(16) Kummel, A. C.; Sitz, G. O.; Zare, R. N. *J. Chem. Phys.* **1986**, *85*, 6874.
(17) Kummel, A. C.; Sitz, G. O.; Zare, R. N. *J. Chem. Phys.* **1988**, *88*, 6707.
(18) Kummel, A. C.; Sitz, G. O.; Zare, R. N. *J. Chem. Phys.* **1988**, *88*, 7357.
(19) Waldeck, J. R.; Kummel, A. C.; Sitz, G. O.; Zare, R. N. *J. Chem. Phys.* **1989**, *90*, 4112.
(20) Green, F.; Hancock, G.; Orr-Ewing, A. J.; Brouard, M.; Duxon, S. P.; Enriquez, P. A.; Sayos, R.; Simons, J. P. *Chem. Phys. Lett.* **1991**, *182*, 568.
(21) Brouard, M.; Duxon, S. P.; Enriquez, P. A.; Sayos, R.; Simons, J. P. *J. Phys. Chem.* **1991**, *95*, 8169.
(22) Brouard, M.; Duxon, S. P.; Enriquez, P. A.; Simons, J. P. *J. Chem. Phys.* **1992**, *97*, 7414.
(23) Costen, M. L.; Hancock, G.; Orr-Ewing, A. J.; Summerfield, D. *J. Chem. Phys.* **1994**, *100*, 2754.
(24) Kim, H. L.; Wickramaaratchi, M. A.; Zheng, X.; Hall, G. E. *J. Chem. Phys.* **1994**, *101*, 2033.
(25) Brouard, M.; Lambert, H. M.; Short, J.; Simons, J. P. *J. Phys. Chem.* **1995**, *99*, 13571.
(26) Shafer, N. E.; Orr-Ewing, A. J.; Simpson, W. R.; Xu, H.; Zare, R. N. *Chem. Phys. Lett.* **1993**, *212*, 155.
(27) Simpson, W. R.; Orr-Ewing, A. J.; Zare, R. N. *Chem. Phys. Lett.* **1993**, *212*, 163.
(28) Simpson, W. R.; Orr-Ewing, A. J.; Rakitzis, T. P.; Kandel, S. A.; Zare, R. N. *J. Chem. Phys.* **1995**, *103*, 7299.
(29) Simpson, W. R.; Rakitzis, T. P.; Kandel, S. A.; Orr-Ewing, A. J.; Zare, R. N. *J. Chem. Phys.* **1995**, *103*, 7313.
(30) Shafer, N. E.; Xu, H.; Tuckett, R. P.; Springer, M.; Zare, R. N. *J. Phys. Chem.* **1994**, *98*, 3369.
(31) Shafer-Ray, N. E.; Orr-Ewing, A. J.; Zare, R. N. *J. Phys. Chem.* **1995**, *99*, 7591.
(32) Chandler, D. W.; Houston, P. L. *J. Chem. Phys.* **1987**, *87*, 1445.
(33) Heck, A. J. R.; Chandler, D. W. *Annu. Rev. Phys. Chem.* **1995**, *46*, 335 and references therein.
(34) Chen, K. *Chem. Phys. Lett.* **1992**, *198*, 288.
(35) Chen, K.; Pei, C. *Chem. Phys. Lett.* **1994**, *217*, 471.
(36) Chen, K.; Kuo, C.; Tzeng, M.; Shian, M.; Chung, S. *Chem. Phys. Lett.* **1994**, *221*, 341.
(37) Chen, K.; Sung, C.; Chang, J.; Chung, T.; Lee, K. *Chem. Phys. Lett.* **1995**, *240*, 17.
(38) Chen, K.; Lee, K.; Chang, J.; Sung, C.; Chung, T.; Liu, T.; Perng, H. *J. Phys. Chem.* **1996**, *100*, 488.
(39) Fano, U. *Rev. Mod. Phys.* **1957**, *29*, 74.
(40) Blum, K. *Density Matrix Theory and Applications*; Plenum: New York, 1981.
(41) Zare, R. N. *Angular Momentum*; Wiley: New York, 1988.
(42) Chen, K.; Yeung, E. S. *J. Chem. Phys.* **1979**, *70*, 1312.
(43) Chen, K.; Yeung, E. S. *J. Chem. Phys.* **1979**, *71*, 4941.
(44) Chen, K.; Yeung, E. S. *J. Chem. Phys.* **1980**, *72*, 4723.
(45) McClelland, G. M.; Herschbach, D. R. *J. Phys. Chem.* **1987**, *91*, 5509.
(46) Siebbeles, L. D. A.; Glass-Maujean, M.; Vasyutinskii, O. S.; Beswick, J. A.; Roncero, O. *J. Chem. Phys.* **1994**, *100*, 3610.
(47) Uberna, R.; Hinchliffe, R. D.; Cline, J. I. *J. Chem. Phys.* **1995**, *103*, 7934.
(48) Mo, Y.; Katayanagi, H.; Heaven, M. C.; Suzuki, T. *Phys. Rev. Lett.* **1996**, *77*, 830.
(49) Kinsey, J. L. *J. Chem. Phys.* **1977**, *66*, 2560.
(50) Herman, G. T., Ed. *Image Reconstruction from Projections*; Springer-Verlag: Berlin, 1979.